Eel-Inspired Electrohydraulic Soft Swimmer with Programmable Undulatory Gaits

Yi Jin[1], Imon G. Pranta[1], Yunteng Cao[2], Guiyin Xu[3*], and Changyong (Chase) Cao[1,4,5*], *Senior Member, IEEE*

***Abstract*—Undulatory locomotion in anguilliform swimmers motivates soft robots that are efficient and maneuverable. We present an eel-inspired soft swimmer actuated by liquid-dielectric electrohydraulic actuators (LDEAs) with programmable inter-segment phase for gait control. A resistive-force-theory (RFT) model relates amplitude, frequency, and phase to forward speed and is validated experimentally. Bench tests confirm repeatable bending in air and water. Swimming trials show speed increases with drive frequency, peaking at 22 mm/s at 5 Hz. Phase sweeps indicate that in-phase activation yields the highest forward speed in this three-segment configuration, while traveling-wave gaits provide effective propulsion and enable amplitude-biased turning for left/right maneuvers. Energy metering indicates a minimum dimensionless cost of transport of 54.99. These results demonstrate that LDEAs offer compact, programmable actuation for efficient, controllable soft underwater robots and establish an RFT-guided framework for gait design.**

***Index Terms*—soft robot, swimming robots, liquid-dielectric electrohydraulic actuators (LDEAs), programmable undulatory gaits, anguilliform swimmers**

I. INTRODUCTION

Undulatory locomotion in anguilliform swimmers (order Anguilliformes) achieves high maneuverability and endurance through smooth, head-to-tail body waves [1], [2]. Unlike rigid-bodied fish, the continuous bending of eels enables navigation through narrow crevices, rapid reversals, and long-distance migration. These capabilities have inspired eel-like robots for confined-space exploration [3], [4], infrastructure inspection [5], [6], and studies of mechanical intelligence in nature [7], [8].

Soft actuation is central to reproducing these undulatory motions [9], [10]. Dielectric-elastomer swimmers can generate fast bends but often require kilovolt-level drive and careful encapsulation to achieve large amplitudes in water [11]–[13]. Pneumatic and cable-driven designs provide large stroke and tunable compliance [7], [14], [15], yet typically rely on bulky off-board pumps, valves, or transmissions that add mass and tether complexity [16]–[18]. These trade-offs motivate compact, electrically driven electrohydraulic approaches.

To address these challenges, we develop an eel-inspired soft swimming robot powered by liquid-dielectric electrohydraulic actuators (LDEAs) [19]–[21]. LDEAs convert high-voltage electrostatic forces into pressure redistribution within sealed liquid-dielectric membrane chambers, producing large, rapid, and reversible bending/contractile deformations. Inspired by the biology in Fig. 1(a), we bond three pairs of electrohydraulic actuators onto thin, elongated polyimide (PI) films to create a lightweight segmented body in Fig. 1(b). Under sinusoidal voltage drive, the robot generates biomimetic undulatory motion in water with either synchronized or phase-shifted segment activation.

We derive an analytical hydrodynamic model based on resistive-force theory (RFT) [22], [23] to predict the dependence of swimming speed on actuation frequency and inter-segment phase, and we validate the model experimentally. We further examine how phase-programmable gaits (in-phase vs. traveling-wave) and amplitude asymmetry enable controllable left/right turning. Finally, we quantify energetic performance via the dimensionless cost of transport (COT).

The main contributions of the work include:

1) A compact, segmented LDEA-actuated eel-like swimmer with programmable inter-segment phase (in-phase and traveling-wave gaits); 2) An RFT-based analytical model linking amplitude, frequency, and phase to forward speed, with experimental validation; 3) Systematic gait studies (frequency/phase sweeps) revealing performance trends and a steering method via amplitude bias; 4) Energetic analysis (COT) and implementation details compatible with high-voltage operation in water.

The paper is organized as follows: Section 2 details the actuator/robot design and fabrication. Section 3 derives the hydrodynamic model. Section 4 reports swimming speeds, frequency/phase studies, steering, and COT analysis. Section 5 concludes with limitations and future directions.

II. DESIGN AND FABRICATION

A. Robot Design and Working Principle

The electrohydraulic soft swimmer is inspired by eel undulation and comprises front and rear buoyancy units, a flexible segmented body, and electrohydraulic actuators (Fig. 2(a)).

Manuscript received Sep 27, 2025; accepted Feb XX, 2026. Date of publication Feb XX, 2026; date of current version Feb 12, 2026. This work is partially supported by the U.S. National Science Foundation (ECCS-2024649) and Case Western Reserve University. This article was recommended for publication by Associate Editor XXX and Editor XXX upon evaluation of the reviewers' comments.

[1] Laboratory for Soft Machines & Electronics, Department of Mechanical and Aerospace Engineering, Case Western Reserve University, Cleveland, OH 44106, USA

[2] Department of Molecular, Cellular and Developmental Biology,

[3] State Key Laboratory for Modification of Chemical Fibers and Polymer Materials, College of Materials Science and Engineering, Donghua University, Shanghai 201620, China

[4] Department of Electrical, Computer and Systems Engineering, Case Western Reserve University, Cleveland, OH 44106, USA.

[5] Advanced Platform Technology (APT) Center, Louis Stokes Cleveland VA Medical Center, Cleveland, OH 44106, USA

Correspondence: `ccao@case.edu` (C. Cao), `xuguiyin@dhu.edu.cn` (G. Xu).

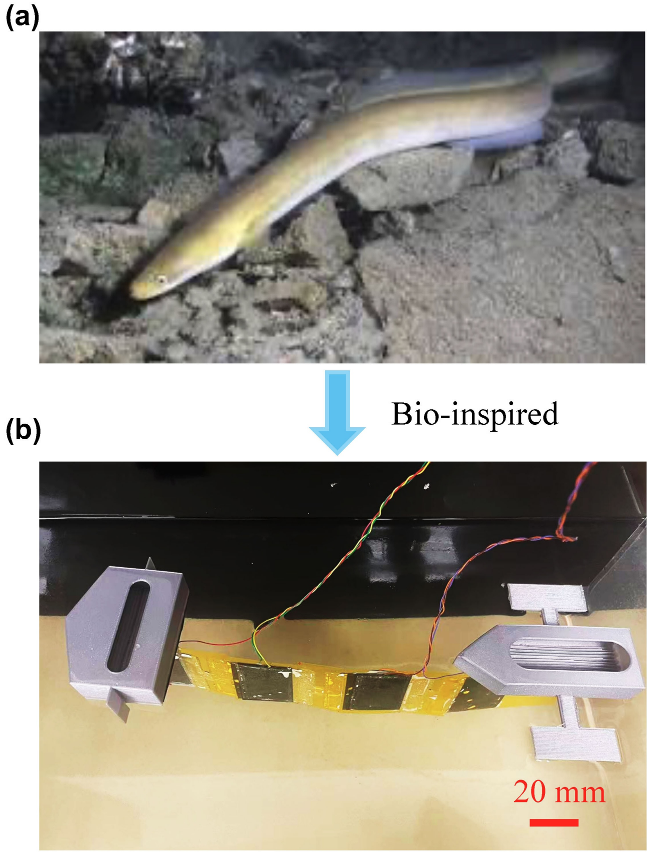

Fig. 1. Eel-inspired electrohydraulic soft swimmer. (a) An eel (anguilliform swimming) in water. (b) Prototype of the LDEA-actuated soft swimmer.

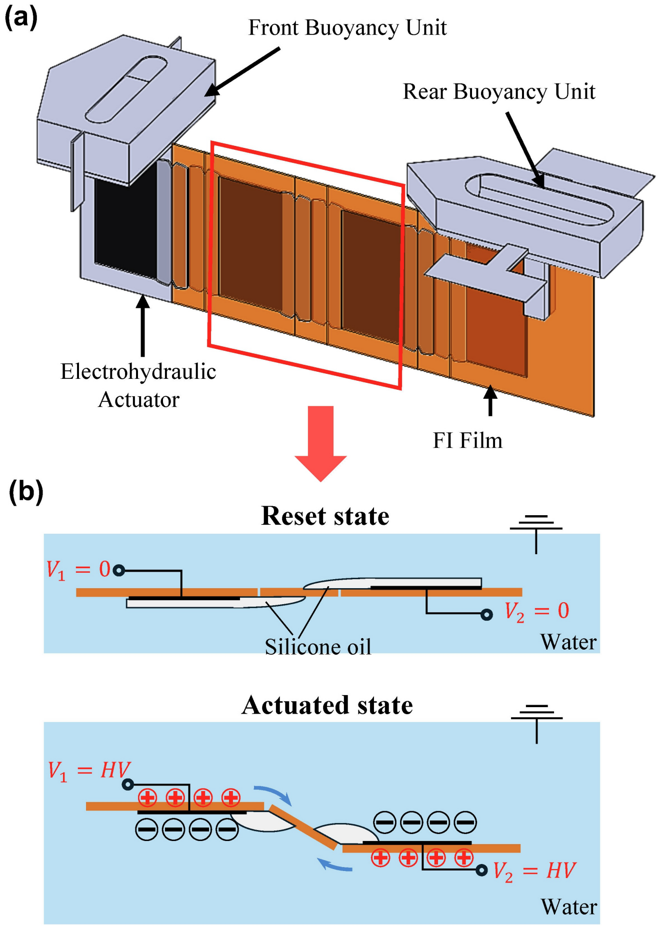

Fig. 2. (a) Schematic showing buoyancy units, head with lateral fins, three PI segments, and left–right LDEAs per segment. (b) Working principle of an asymmetric LDEA pair: Maxwell stress redistributes liquid dielectric; phase-offset activation yields traveling-wave undulation.

The head is a T-shaped plate attached to the front buoyancy unit; two small side fins are integrated to suppress yaw during swimming and thereby reduce hydrodynamic drag. Although these components enhance directional stability, they also alter the local flow field and introduce additional drag, resulting in a trade-off between stability and propulsive efficiency. The main body is fabricated from 0.05-mm-thick polyimide (PI) film and divided into three segments. On each segment, a pair of electrohydraulic actuators is bonded asymmetrically to the two sides to generate bending. To enhance segment bending, the working zones do not overlap within a segment. With actuators arranged on three segments, the robot effectively forms six joints, and actuators on the same side produce bending in the same direction.

Each actuator is a liquid-dielectric electrohydraulic actuator (LDEA) implemented as a sealed membrane chamber (pouch) partially covered on one side by a flexible anode electrode; the surrounding water serves as the cathode. Fig. 2(b) illustrates the operating principle within a single segment. In the reset state (no voltage), the body remains straight. Upon applying voltage to the left/right actuator pair, Maxwell stress redistributes the liquid dielectric into the working zone, causing the two actuators to bend in opposite directions and inducing an S-shaped body profile. By serially connecting the three segments and applying phase-shifted sinusoidal voltages, the body generates a traveling-wave undulation for propulsion. When the voltage is removed, the actuators relax and the body returns to the reset (straight) state.

B. Fabrication Process

Figure 3 summarizes the fabrication of the electrohydraulic actuators and the swimmer, following the methods described in the literature [24]. Each actuator is formed by heat-sealing two BOPP films (biaxially oriented polypropylene, Generic) to create a liquid-tight chamber. Sealing is performed using a 3D printer as the heated tool while the two sealable sides of the BOPP films face each other and are sandwiched between Kapton sheets to ensure uniform pressure and protect the films (Fig. 3(a)). The chamber geometry is specified as $h \times w \times r$ (Fig. 3(b)), and a fill port is reserved for subsequent liquid-dielectric filling. After sealing, each pouch is trimmed along the seal edge to achieve clean boundaries.

A flexible anode electrode is then applied by brushing carbon ink (CL-2051, Nagase ChemteX America Corp.) onto one side of the sealed chamber (Fig. 3(c)). The chamber is filled via the port with silicone oil (5 cSt, Sigma-Aldrich Ltd.) as the liquid dielectric using a syringe, and the port is hermetically closed with a soldering iron (Fig. 3(d), Fig. 3(e)).

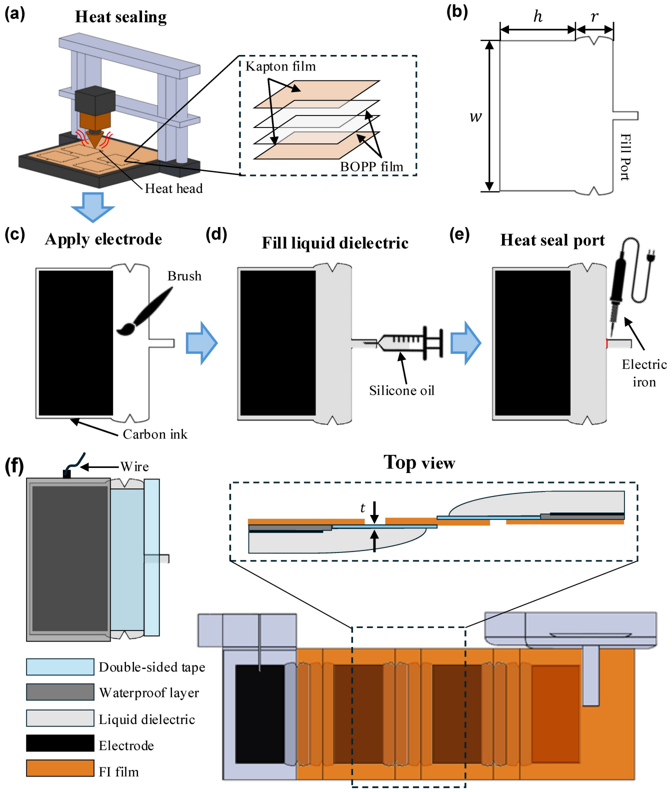

Fig. 3. Fabrication workflow: (a) heat-seal BOPP films to form chamber; (b) chamber dimensions $h \times w \times r$; (c) trim and apply carbon-ink electrode; (d) fill with silicone oil; (e) hermetically seal port; (f) waterproof, attach lead, define working zone, assemble three asymmetric actuator pairs on Kapton backbone.

To improve waterproofing and provide mechanical protection, the electrode side is encapsulated with 0.6-mm-thick double-sided tape (3M, VHB 5295), and a lead wire is attached to the electrode to enable the high-voltage connection. The actuator's working zone is further defined and reinforced by overlaying a thin double-sided adhesive layer (t = 0.05 mm).

For body assembly, the Kapton film backbone (Kapton tape, Gizmo Dorks) is cut into separate pieces corresponding to the three segments and joined by the actuators (Fig. 3(f)). At each joint, a small gap is left between adjacent PI pieces to reduce bending stiffness and facilitate smooth actuation. The assembled segments, together with the front and rear buoyancy units and the T-shaped head plate with side fins described in Section 2.1, complete the swimmer architecture.

III. CHARACTERIZATION AND ANALYSIS

In our swimmer, each LDEA is laminated to a compliant PI substrate to realize large, smooth bending compatible with segmented undulation. Unlike prior designs on rigid or semi-rigid backings, this configuration increases structural compliance and better matches the distributed deformation required for underwater locomotion. We first characterize LDEA bending in air and water to quantify fluid-loading effects. Building on these results, we develop an analytical hydrodynamic model that links actuator kinematics to thrust and forward speed.

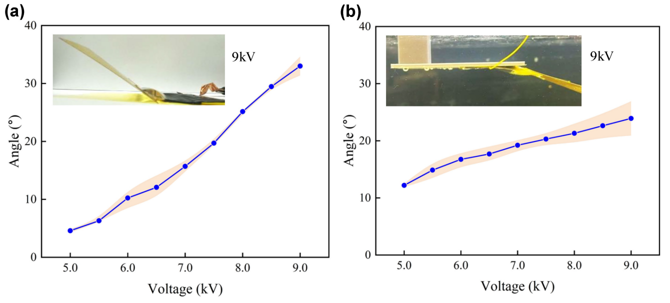

Fig. 4. LDEA bending performance. (a) Voltage–bending-angle characterization in air. (b) In water (approximately linear in both cases; peak angles reduced in water).

TABLE I
PARAMETERS OF THE LIQUID-DIELECTRIC ELECTROHYDRAULIC ACTUATORS (LDEAS) AND EEL-INSPIRED SWIMMER.

Quantity	Value	Quantity	Value
w	60 mm	l_h	45 mm
h	30 mm	l_{b1}	15 mm
r	15 mm	l_{b2}	45 mm
ε_r	2.2	l_t	45 mm

A. LDEA Performance in Air and Water

The tested LDEA has nominal dimensions 30 × 60 × 15 mm (Table 1), corresponding to a silicone-oil fill volume of 3.5 mL. Following Section 2.2, we measured the voltage–bending-angle relation in air and water. For air tests, the LDEA was placed in front of a camera; the applied voltage was increased from 5 kV to 9 kV in 0.5 kV steps with images recorded at each step. Measurements were repeated three times. Bending angles were quantified in ImageJ. For water tests, the LDEA was partially bonded to a rigid plate and mounted upside down, with the electrode-free surface facing downward so that the surrounding water served as the cathode, improving coupling while mitigating short-circuit risk.

Figs. 4(a-b) show an approximately linear voltage–angle relationship in air and water. In air, the LDEA reached a maximum bending angle of 35° at 9 kV; in water, the maximum decreased to 25° due to hydrodynamic resistance. Relative to electrohydraulic actuators mounted on rigid substrates, the compliant substrate yields a lower peak angle because part of the deformation is absorbed by the backing; however, the achieved angles are sufficient for the required undulatory body motion. The compliant backing also improves bend smoothness, integration with the segmented body, and biomimetic compliance.

B. Hydrodynamic Modeling and Analysis

We model the three-segment swimmer as a serial chain with six joints (Fig. 5(a)), each joint corresponding to an LDEA. Because each segment carries a left–right asymmetric pair, we denote left-side joints as A_i^L, (i = 1,2,3) and right-side joints as A_i^R, (i = 1,2,3). The head length l_h, and intra-pair spacings l_{12}, l_{23}, and tail length l_t are listed in Table I.

Segments receive sinusoidal voltages with phase offsets. When the input to segment i is positive, joint A_i^L rotates; when negative, joint A_i^R rotates. The segment bend is modeled as

$$\theta_i(t) = A\sin\big(2\pi f t + \phi_i\big), \quad i = 1, 2, 3. \tag{1}$$

where A is the bend amplitude (set by the applied voltage), f is the drive frequency, and ϕ_i is the phase.

Using resistive-force theory (RFT) [25], under small-amplitude assumptions, the cycle-averaged thrust scales with amplitude squared and angular frequency squared,

$$F_{\text{thrust}} = cA^2(2\pi f)^2 \tag{2}$$

where c is a thrust force coefficient related to geometry, fluid density, and drag anisotropy. For the speed range considered, we use a linearized drag

$$F_{\text{drag}} = k_{\text{drag}}\,|v| \tag{3}$$

So the net force is $F_{net} = F_{thrust} - F_{drag}$. With effective mass m (robot + added mass), the discrete forward-speed update is

$$v(t+\Delta t) = v(t) + \frac{F_{\text{net}}}{m}\,\Delta t \tag{4}$$

and the displacement evolves as

$$X(t+\Delta t) = X(t) + v(t+\Delta t)\,\Delta t \tag{5}$$

Body configurations follow from the forward kinematics of the 6-joint chain using $\theta_i(t)$ from (1). For the traveling-wave gait with $\phi_1 = 0$, $\phi_2 = 2\pi/3$, $\phi_3 = 4\pi/3$ and amplitude set by 9 kV, Figs. 5(b)–(d) shows representative shapes at t= 0.8, 1.6, 2.4, 3.2, and 4.0 s for f=1, 2, and 5 Hz. The displacement-time curves (Fig. 5(e)) are nonlinear and exhibit increasing average speed with frequency, consistent with the A² f² scaling in (2). In practice, c, k_{drag}, and m are identified by fitting model trajectories to experimental data. Our current model is based on the assumptions of small bending angles, linear drag, and constant amplitude. However, the experiments in Section 4 demonstrate that the amplitude decreases at high frequencies because the LDEA cannot fully recover. When operating at higher Reynolds numbers and actuation frequencies, a quadratic drag term F_{drag} & $v|v|$ and a frequency-dependent amplitude $A(v, f)$ obtained from experimental and simulation data and captured using machine-learning techniques can be incorporated into the model.

IV. PERFORMANCE EVALUATION OF THE EEL-LIKE SWIMMING ROBOT

We experimentally evaluate the eel-like swimmer's forward speed, the effects of frequency and phase offset on speed and cost of transport (COT), and its maneuverability via amplitude-biased control. Measured trajectories are compared against analytical predictions.

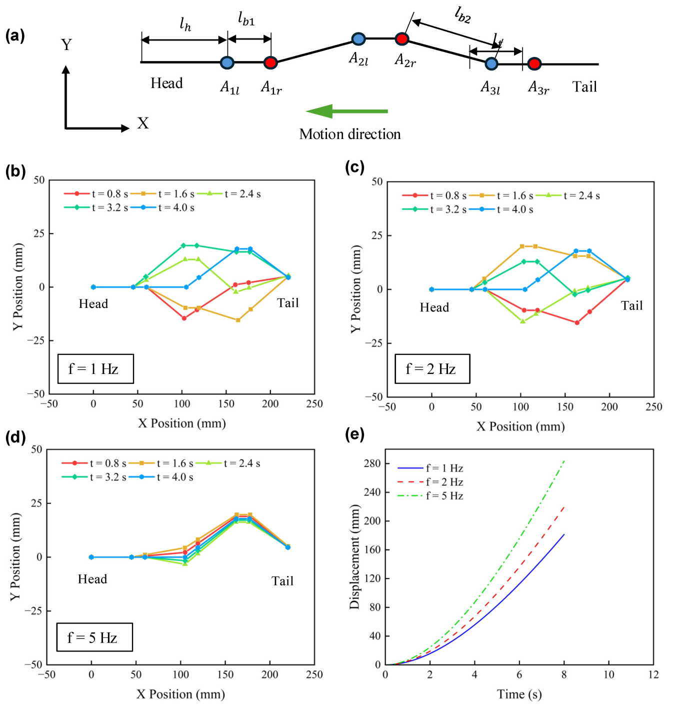

Fig. 5. Analytical model and simulated body configurations. (a) Three-segment, six-joint model. (b) Simulated postures at $f = 1\,\text{Hz}$. (c) $f = 2\,\text{Hz}$. (d) $f = 5\,\text{Hz}$. In (b–d), $\boldsymbol{\phi} = [0, 2\pi/3, 4\pi/3]$, $V = 9\,\text{kV}$. (e) Model-predicted displacement–time curves showing increased average speed with frequency.

A. Swimming Speed Tests

The test setup is shown in Fig. 6(a). The robot swam in a water tank with a tape measure affixed to the outside wall along the swimming direction to quantify displacement. A front-view camera recorded motion and timing for speed estimation, while a top-view camera captured body configurations and was also used for maneuverability tests. High voltage was supplied by a multi-channel HV controller (PS2-08-A, Artimus Robotics; 8 channels), with six channels programmed to deliver sinusoidal drive signals to the LDEAs.

In the first study, we examined the effect of frequency on swimming speed using a traveling-wave gait with phase offsets $\phi_1 = 0$, $\phi_2 = 2\pi/3$, $\phi_3 = 4\pi/3$ and 9 kV amplitude. From the video, displacement-time traces were extracted and are plotted in Fig. 6(b) for f=1,2,5 Hz. The displacement–time relationships are nonlinear, and the average speed increases with frequency. At f=5Hz, the robot reaches a maximum speed of 22 mm/s. The speeds for f=1 Hz and f=2 Hz are 18.71 mm/s and 19.18 mm/s, respectively. Analytical predictions (Section 3; see Fig. S1(a–c)) were compared against measurements; the RMSE values between prediction and experiment are 20.81, 30.25, and 36.59 (units consistent with displacement, e.g., mm) for f=1,2,5 Hz, respectively.

For t¡= 5s, the analytical curves closely follow the experimental trends, confirming the model's accuracy in the initial phase. At longer times and especially at higher frequencies, deviations grow because the LDEAs do not fully recover between cycles, reducing the effective oscillation amplitude, whereas the model assumes constant amplitude. Additionally,

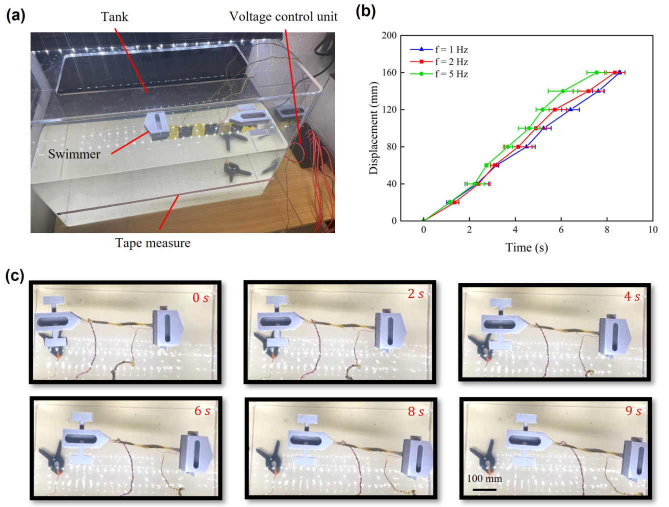

Fig. 6. Swimming-speed tests at different frequencies. (a) Setup with tape measure, front/top cameras, and 8-channel HV controller (PS2-08-A); six channels drive LDEAs. (b) Measured displacement–time curves for $f = \{1, 2, 5\}$ Hz under $\phi = [0, 2\pi/3, 4\pi/3]$, $V = 9\,\text{kV}$. (c) Straight-swimming demonstration at $f = 2\,\text{Hz}$.

residual head motion increases hydrodynamic resistance in the experiment but is not captured in the simplified model. Representative body configurations at f=2Hz are shown in Fig. 6(c).

B. Influence of Phase Offset on Swimming Speed

We next evaluated the effect of inter-segment phase on speed at fixed f=2 Hz and 9 kV:

- Phase 1: $\phi_1 = 0$, $\phi_2 = 0$, $\phi_3 = 0$ (all in-phase),
- Phase 2: $\phi_1 = 0$, $\phi_2 = \pi/2$, $\phi_3 = \pi$,
- Phase 3: $\phi_1 = 0$, $\phi_2 = 2\pi/3$, $\phi_3 = 4\pi/3$ (traveling-wave).

The corresponding control signals are in Fig. 7(a–c), and the measured speeds are compared in Fig. 7(d). The maximum speed occurs for Phase 1 (in-phase), 22.13 mm/s. Phase 3 yields 19.18 mm/s, close to Phase 1, while Phase 2 produces 14.36 mm/s. In Phase 1, synchronous bending produces strong, consistent rearward thrust with minimal cancellation. In Phase 2, intermediate phase lags lead to partial destructive interference—one segment thrusts while another recovers—reducing net propulsion. Phase 3 establishes a traveling wave that remains effective but dissipates some energy in lateral oscillations, giving a speed slightly below the in-phase case for this three-segment morphology. Another reason is that three segments are insufficient to form an effective traveling wave, thereby reducing wave-based thrust. In-phase motion instead maximizes synchronized body motion and added-mass thrust. With more segments, a smoother traveling wave could develop and may outperform in-phase motion.

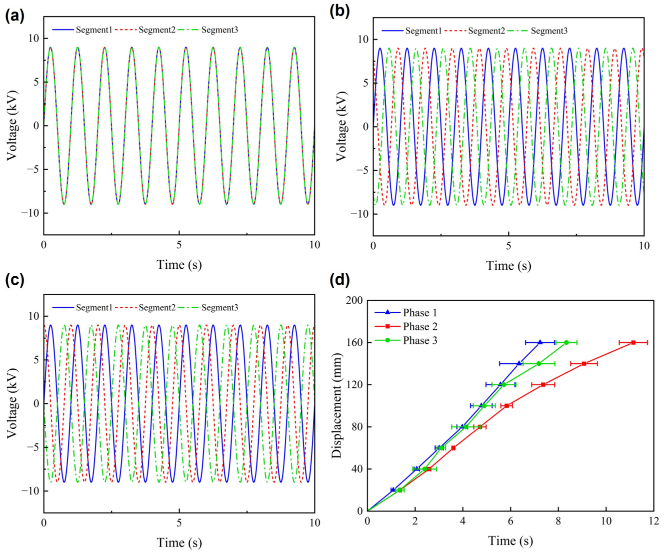

Fig. 7. Effect of inter-segment phase on speed at $f = 2\,\text{Hz}$, $V = 9\,\text{kV}$. (a) Phase 1: $[0, 0, 0]$. (b) Phase 2: $[0, \pi/2, \pi]$. (c) Phase 3: $[0, 2\pi/3, 4\pi/3]$. (d) Measured average speeds: 22.13, 19.18, and 14.36 mm/s for Phases 1, 3, and 2, respectively.

TABLE II

ENERGY AND DIMENSIONLESS COST OF TRANSPORT (COT) ACROSS FREQUENCIES AND PHASE OFFSETS. VALUES ARE REPORTED AS MEAN ± STANDARD DEVIATION OVER THREE TRIALS.

Control Signal	**Energy (J)**	**COT**	**Trials**
Phase 3, $f = 1\ Hz$	4.89 ± 0.03	65.03 ± 0.33	3
Phase 3, $f = 2\ Hz$	4.78 ± 0.22	63.43 ± 2.92	3
Phase 3, $f = 5\ Hz$	4.32 ± 0.21	57.34 ± 2.83	3
Phase 1, $f = 2\ Hz$	4.14 ± 0.21	54.99 ± 2.88	3
Phase 2, $f = 2\ Hz$	6.38 ± 0.48	84.72 ± 6.31	3

C. Cost of Transport

We quantify energetic efficiency using the dimensionless cost of transport (COT),

$$COT = \frac{E}{mgd} \tag{6}$$

where E is the total electrical energy consumed, m the robot mass, g gravitational acceleration, and d the distance traveled. COT enables comparison across scales and platforms: lower COT => less energy per unit weight per unit distance.

Using the experimental data from Sections 4.1 and 4.2 (see Table S1 for parameters), we computed energy consumption and COT under each control condition, where the applied voltage was prescribed by the controller and the RMS current was measured experimentally using a multimeter connected in series with the actuator. Table II summarizes the results. The robot consumed $5J$ to travel 160 mm. The lowest COT occurred for $f = 2$ Hz, Phase 1, with $COT = 54.99$; the other conditions yielded COT values near 60. These results indicate that the swimmer achieves relatively efficient locomotion for an electrohydraulically actuated soft platform.

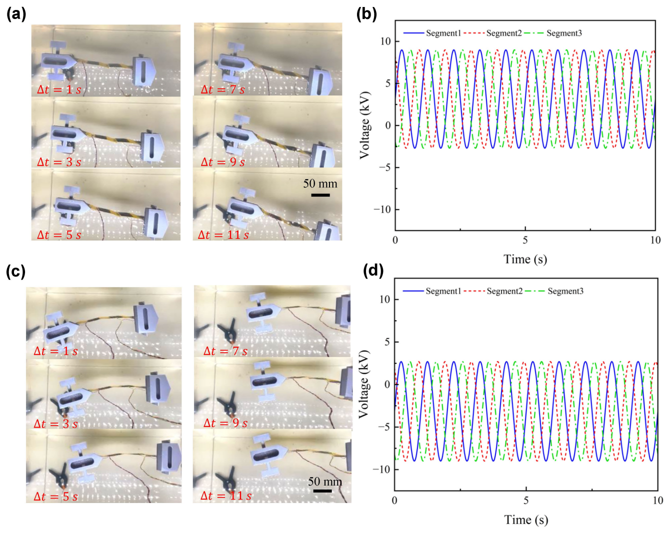

Fig. 8. Maneuverability via amplitude-biased control. (a) Right turn with left-biased actuation ($A_L > A_R$). (b) Corresponding inputs. (c) Left turn with right-biased actuation ($A_R > A_L$). (d) Corresponding inputs.

D. Maneuverability Test

Directional control is achieved by amplitude-biased actuation between the left and right LDEAs on each segment. Let $\omega = 2\pi f$. We command

$$\theta_i(t) = A_L \sin(\omega t + \phi_i) - A_R \sin(\omega t + \phi_i), \quad i = 1, 2, 3 \quad (7)$$

where A_L and A_R are the left and right actuation amplitudes, respectively. When $A_L > A_R$, the waveform is left-biased and the swimmer turns right; when $A_R > A_L$, the bias reverses and the swimmer turns left. Fig. 8(a) shows a right turn produced by a left-biased signal [Fig. 8(b)]; Fig. 8(c) shows a left turn under a right-biased signal [Fig. 8(d)]. These tests confirm that differential amplitude control provides an effective steering mechanism for the eel-like swimmer.

V. CONCLUSION

We presented an eel-inspired soft swimmer actuated by liquid-dielectric electrohydraulic actuators and validated its performance through modeling and experiments. A lightweight, three-segment design with phase-programmable gaits achieved biomimetic undulation. An analytical model based on resistive-force theory linked amplitude, frequency, and phase to forward speed and matched measurements well in the initial regime; deviations after 5 s arose from frequency-dependent amplitude recovery and residual head motion not captured by the constant-amplitude assumption. Experiments showed that increasing driving frequency improved performance, with a maximum speed of 22.13 mm s^{1} at 5 Hz. Phase-offset studies revealed that in-phase activation produced the highest thrust and speed, a traveling-wave gait yielded a slightly lower but still effective 19.18 mm s^{1}, and a (0, /2,) pattern with partial interference reduced speed to 14.36 mm s^{1}. Energetic analysis indicated the robot consumed 5 J over 160 mm of travel, with a minimum dimensionless COT of 54.99 under the f=2 Hz, in-phase condition. Maneuverability tests confirmed that amplitude asymmetry between left and right LDEAs provides effective directional control. The present model assumes constant amplitude and linear drag; extending it to include amplitude dynamics and quadratic drag at higher Re should improve long-horizon accuracy. Further efficiency gains may come from phase-lag optimization, tether/fin ablation to quantify parasitics, and packaging refinements to reduce losses. Integrating onboard power and control, adding onboard sensing for closed-loop gait regulation, and conducting durability and safety evaluations for prolonged high-voltage operation in water are the immediate next steps toward fully autonomous underwater soft robots; these efforts will require compact high-voltage power electronics, lightweight energy storage, robust insulation strategies, and careful management of the trade-off between added mass and swimming performance.

REFERENCES

[1] G. Li, G. Liu, D. Leng, X. Fang, G. Li, and W. Wang, "Underwater undulating propulsion biomimetic robots: A review," *Biomimetics*, vol. 8, no. 3, p. 318, Jul. 2023.

[2] V. Stin, R. Godoy-Diana, X. Bonnet, and A. Herrel, "Form and function of anguilliform swimming," *Biol. Rev. Camb. Philos. Soc.*, vol. 99, no. 6, pp. 2190–2210, Dec. 2024.

[3] G. Bianchi, L. Lanzetti, D. Mariana, and S. Cinquemani, "Bioinspired design and experimental validation of an aquatic snake robot," *Biomimetics*, vol. 9, no. 2, p. 87, Feb. 2024.

[4] T. S. Vaquero, et al., "EELS: Autonomous snake-like robot with task and motion planning capabilities for ice world exploration," *Sci. Robot.*, vol. 9, no. 88, p. eadh8332, Mar. 2024.

[5] E. Kelasidi, P. Liljebäck, K. Y. Pettersen, and J. T. Gravdahl, "Experimental investigation of efficient locomotion of underwater snake robots for lateral undulation and eel-like motion patterns," *Robot. Biomim.*, vol. 2, p. 8, Dec. 2015.

[6] F. Lyu, X. Xu, X. Zha, Z. Li, and H. Yuan, "A snake eel inspired multi-joint underwater inspection robot for undersea infrastructure intelligent maintenance," in *Proc. OCEANS 2022*, Chennai, India, 2022, pp. 1–5.

[7] M. Fernandez, T. Wang, G. Tunnicliffe, D. Dortilus, P. Gunnarson, J. O. Dabiri, and D. I. Goldman, "AquaMILR+: Design of an untethered limbless robot for complex aquatic terrain navigation," *arXiv:2409.18383 [cs.RO]*, 2024.

[8] Q. Wang, Z. Hong, and Y. Zhong, "Learn to swim: Online motion control of an underactuated robotic eel based on deep reinforcement learning," *Biomim. Intell. Robot.*, vol. 2, no. 4, p. 100066, Dec. 2022.

[9] C. D. Onal and D. Rus, "Autonomous undulatory serpentine locomotion utilizing body dynamics of a fluidic soft robot," *Bioinspir. Biomim.*, vol. 8, no. 2, p. 026003, Jun. 2013.

[10] A. Jusufi, D. M. Vogt, R. J. Wood, and G. V. Lauder, "Undulatory swimming performance and body stiffness modulation in a soft robotic fish-inspired physical model," *Soft Robot.*, vol. 4, no. 3, pp. 202–210, Sep. 2017.

[11] C. Zhang, "An eel-like robot based on a dielectric elastomer," *PLoS ONE*, vol. 20, no. 7, p. e0324738, Jul. 2025.

[12] E. Hajiesmaili and D. R. Clarke, "Dielectric elastomer actuators," *J. Appl. Phys.*, vol. 129, no. 15, p. 151102, Apr. 2021.

[13] M. Wissler and E. Mazza, "Modeling and simulation of dielectric elastomer actuators," *Smart Mater. Struct.*, vol. 14, no. 6, p. 1396, Dec. 2005.

[14] D. Q. Nguyen and V. A. Ho, "Anguilliform swimming performance of an eel-inspired soft robot," *Soft Robot.*, vol. 9, no. 3, pp. 425–439, Jun. 2022.

[15] K. Suzumori, S. Endo, T. Kanda, N. Kato, and H. Suzuki, "A bending pneumatic rubber actuator realizing soft-bodied manta swimming robot," in *Proc. IEEE Int. Conf. on Robotics and Automation (ICRA)*, Rome, Italy, 2007, pp. 4975–4980.

[16] Y. Zhao, W. Zhao, M. Song, M. S. Islam, Z. Liu, X. Liu, and C. Cao, "Self-adaptive, untethered soft gripper system for efficient agricultural harvesting," *J. Field Robot.*, in press, 2024.

[17] X. Liu, M. Song, Y. Fang, Y. Zhao, and C. Cao, "Worm-inspired soft robots enable adaptable pipeline and tunnel inspection," *Adv. Intell. Syst.*, vol. 4, no. 1, p. 2100128, Jan. 2022.

[18] S. Chen, Y. Pang, H. Yuan, X. Tan, and C. Cao, “Soft robotic manipulation system capable of stiffness variation and dexterous operation for safe human–machine interactions,” *Adv. Mater. Technol.*, vol. 6, no. 5, p. 2100084, May 2021.

[19] E. Acome, S. K. Mitchell, T. G. Morrissey, M. B. Emmett, C. Benjamin, M. King, M. Radakovitz, and C. Keplinger, “Hydraulically amplified self-healing electrostatic actuators with muscle-like performance,” *Science*, vol. 359, no. 6371, pp. 61–65, Jan. 2018.

[20] T. Wang, H.-J. Joo, S. Song, W. Hu, C. Keplinger, and M. Sitti, “A versatile jellyfish-like robotic platform for effective underwater propulsion and manipulation,” *Sci. Adv.*, vol. 9, no. 15, p. eadg0292, Apr. 2023.

[21] N. Kellaris, P. Rothemund, Y. Zeng, S. K. Mitchell, G. M. Smith, K. Jayaram, and C. Keplinger, “Spider-inspired electrohydraulic actuators for fast, soft-actuated joints,” *Adv. Sci.*, vol. 8, no. 14, p. 2100916, Jul. 2021.

[22] T. Ming and Y. Ding, “Transition and formation of the torque pattern of undulatory locomotion in resistive force dominated media,” *Bioinspir. Biomim.*, vol. 13, no. 4, p. 046001, May 2018.

[23] T. Zhang and D. I. Goldman, “The effectiveness of resistive force theory in granular locomotion,” *Phys. Fluids*, vol. 26, no. 10, p. 101308, Oct. 2014.

[24] S. K. Mitchell, X. Wang, E. Acome, T. Martin, K. Ly, N. Kellaris, V. G. Venkata, and C. Keplinger, “An easy-to-implement toolkit to create versatile and high-performance HASEL actuators for untethered soft robots,” *Adv. Sci.*, vol. 6, no. 14, p. 1900178, Jul. 2019.

[25] J. Gray and G. J. Hancock, “The propulsion of sea-urchin spermatozoa,” *J. Exp. Biol.*, vol. 32, no. 4, pp. 802–814, Dec. 1955.